CONFERENCE PRE-PRINT

TEM TURBULENCE AND TRANSPORT DEPENDENCE ON L_{T_e} AND L_{n_e} IN EAST WITH $T_e/T_i \sim 1-2$

P Li[1], N Sun[1,2], Y F He[1,2], J P Qian[1], X Jian[1], J L Chen[1], Y Lei[1], G S Li[1], M Q Wu[1] and J G Li[1]
[1]Institute of Plasma Physics of Chinese Academy of Science, Hefei 230031, People's Republic of China
[2]University of Science and Technology of China, Hefei 230026, People's Republic of China
Email: lipan@ipp.ac.cn, ning.sun@ipp.ac.cn

Abstract

Enhanced electron heat transport was observed in the Experimental Advanced Superconducting Tokamak (EAST) H-mode plasmas as R/LT_e increased and R/Ln_e decreased at $Te/Ti \sim$ 1–2. Trapped-Gyro–Landau-Fluid (TGLF) simulations imply the development of high-k TEM and the suppression of low-k TEM, consistent with density-fluctuation measurements from the poloidal correlation reflectometer (PCR) and collective Thomson scattering (CTS) systems. Joint ONETWO and TGLF transport analyses show that these changes in turbulence correspond to an increase in electron heat flux and a reduction in ion heat and particle flux. Compared with low-k TEM, high-k TEM drives stronger electron heat transport, whereas low-k TEM produces stronger outward particle transport. Experimental identification of TEM turbulence and transport analysis are crucial for understanding transport in burning plasma dominated by electron heating with $Te/Ti \sim$ 1–2.

1. INTRODUCTION

Particle and energy losses driven by anomalous transport remain a key limitation on plasma confinement. Broadband drift-wave turbulence is a principal driver of anomalous transport. Drift-wave turbulence is commonly divided into the ion-temperature-gradient (ITG), trapped-electron-mode (TEM) and electron-temperature-gradient (ETG). While TEM exhibits an intermediate-scale character and shows regime-dependent transport responses that vary with multiple control parameters—including the density and temperature gradient scale lengths L_{n_e} and the electron-to-ion temperature ratio T_e/T_i.

Trapped-electron modes (TEM) can influence electron heat, ion heat, and particle transport. Evidence from multiple devices and models supports this view. Nonlinear gyrokinetic simulations show that TEM turbulence can dominate electron heat transport on Alcator C-Mod. TGLF modelling indicates that as high-k components strengthen, the fraction of electron energy flux increases on DIII-D. GTS simulations suggest that dissipative TEM (DTEM) can simultaneously drive both electron and ion energy transport on NSTX. In the particle channel, TEM is frequently associated with a sizeable electron particle flux. For example, direct observations on DIII-D indicate that a short-wavelength, T_e-gradient-driven pinch is a key mechanism by which TEM affects particle transport. Numerical simulations further suggest that electron particle flux is large in TEM-dominated regimes, whereas flux suppression and even reversal can occur across turbulence-regime transition regions.

TEM can be classified into density-gradient–driven (∇n_e-TEM) and electron-temperature-gradient–driven (∇T_e-TEM) variants, among others. At ion scales, the density-gradient–driven TEM tends to be more sensitive to particle flux at lower $k_y\rho_s$ and is modulated by R/L_n. The electron-temperature-gradient–driven TEM is more sensitive to R/L_{T_e} and can contribute substantial electron heat flux at comparatively higher k. The precise k windows depend on device and plasma parameters and should be established by joint experimental–simulation validation. Notably, multiple drives commonly coexist and interconvert in experiments. Consequently, introducing explicit wavenumber bands in experimental analysis facilitates comparison between diagnostic spectra and linear instability spectra. Guided by the subsequent experimental results, we introduce the following criterion in this paper: the modes with $k_\theta\rho_s \lesssim 1$ are considered low-k TEM, while those with $k_\theta\rho_s \gtrsim 1$ are considered as high-k TEM.

TEM branches with differing characteristics can couple and interconvert as control parameters vary. On ASDEX Upgrade, experiments and modelling show that at low collisionality TEM becomes progressively stabilised as collisionality increases, and is supplanted by ITG. These couplings furnish a dynamical pathway for the seesaw between low-k and high-k TEM components. On NSTX, the transition from collisionless TEM (CTEM) to dissipative TEM (DTEM) has also been investigated. However, experimental observations that resolve multiple k-band TEM components within the same spatial region remain scarce, and direct evidence for branch coupling and differential evolution in the gradient region is particularly lacking.

Acquiring such evidence requires diagnostics capable of broadband wavenumber measurements within the same spatial region. Coherent Thomson scattering (CTS) is a common tool for turbulence monitoring. Owing to different emitters and operating bands, systems differ in wavenumber coverage, radial localisation, and scattering geometry. For example, DIII-D employs a 288 GHz far-infrared (FIR) system and a 94 GHz millimetre-wave backscattering system, while ASDEX Upgrade uses microwave Doppler backscattering (DBS). To achieve simultaneous, cross-scale observations within the same core region, the CO_2-CTS system on EAST offers clear advantages and satisfies the observational requirements of this study.

Motivated by the above, we performed simultaneous, same-region broadband measurements of turbulence in the gradient zone using CO_2-CTS under nearly steady auxiliary heating. In conjunction with TGLF linear instability spectra and ONETWO-based inversions, we analysed the temporal evolution of low-k and high-k TEM intensities and their co-variation with key gradient parameters, including R/L_{n_e}, R/L_{T_e}, and T_e/T_i. The experimental findings agree with linear-stability predictions regarding the dominant modes and k ranges, and are corroborated by transport-flux–based inversions. Accordingly, this work provides direct experimental evidence for the differential evolution of cross-scale TEM, and outlines a viable physics pathway for reactor-relevant profile control—via modulation of key gradients such as R/L_{n_e} and R/L_{T_e}—to optimise multiscale turbulence and improve overall confinement.

The experimental device and diagnostic systems are introduced in Section 2. Section 3 presents experimental observations of broad wavenumber multi-scale turbulence evolution. Section 4 analyzes simulation results of the low-k TEM attenuation concomitant with the high-k TEM enhancement. Section 5 provides a conclusion.

2. EXPERIMENTAL SETUP AND MULTI-SCALE TURBULENCE DIAGNOSTIC CAPABILITIES

This study was conducted on the EAST tokamak. EAST is a high-power, long-pulse device with major radius $R \approx 1.85\,\mathrm{m}$ and minor radius $a \approx 0.45\,\mathrm{m}$; its heating and current-drive systems include Ohmic Heating (OH), Lower Hybrid Wave (LHW), Electron Cyclotron resonance heating (EC), Ion Cyclotron resonance heating (IC), and Neutral Beam Injection (NBI). We analyse the density ramp-up phase with combined EC ($\sim 2.8\,\mathrm{MW}$) and NBI-2R (acceleration voltage $\sim 60\,\mathrm{kV}$) heating as the comparison window, ensuring a nearly steady auxiliary power level. For consistency with the linear spectra and transport inversions in Section 3, we adopt the radial region $\rho = r/a \in [0, 1]$, with $\rho = 0$ at the magnetic axis and $\rho = 1$ at the plasma boundary.

We employ the CO_2 coherent Thomson scattering (CO_2-CTS) diagnostic to observe the spatio-temporal evolution of broad wavenumber turbulence. Developed by the Y. D. Li team of EAST, the system has undergone nearly two decades and is technically mature and operationally stable. In this work, we use a self-developed CO_2 laser that delivers a stable TEM_{00} mode at $\sim$ 28 THz. This frequency is well above the plasma characteristic frequency, so refraction and diffraction effects are negligible. In 2024, a major upgrade of CO_2-CTS enhanced ion-scale measurement capability in the gradient region ($\rho \approx 0.4 - 0.8$). The diagnostic covers two representative radial regions ($\rho \approx 0 - 0.4$ and $\rho \approx 0.4 - 0.8$), enabling simultaneous access to electron- and ion-scale spectra, with a typical dimensionless wavenumber range $k_\theta \rho_s \approx 0.5 - 5$. The sampling rate can reach 6 MHz. The CO_2-CTS system has been used on EAST, HT-7, and HL-2A tokamaks for analyses of density fluctuations, and it provides a key measurement capability for our research on cross-scale turbulence observations.

To support the analysis of the turbulence results, we employ auxiliary diagnostics: line-averaged density from an HCN interferometer; electron-density profiles from POINT polarimetry-interferometry and reflectometry; electron temperature from electron-cyclotron-emission (ECE) radiometry; and ion temperature from an X-ray crystal spectrometer (XCS). Because charge-exchange recombination spectroscopy (CXRS) relies on the NBI-2L beam, edge ion-temperature measurements are unavailable when that beam is not in use.

3. EXPERIMENTAL OBSERVATION OF EVOLUTION FROM THE LOW-K-TEM SUPPRESSION TO THE HIGH-K-TEM ENHANCEMENT

Discharge #138384 is analyzed over 4.32–4.37 s. During this time, four ECRH beams were applied (total power $\sim 2.8\ \mathrm{MW}$) together with one NBI-2R beam ($\sim 1.5\ \mathrm{MW}$). Fig. 1 shows the evolution of key plasma parameters: (a) line-averaged density n_e ($10^{19}\ \mathrm{m}^{-3}$); (b) plasma stored energy W_{MHD} (kJ); (c) confinement quality factor $H_{98(y,2)}$; (d) ion temperature T_i (keV); (e) electron temperature T_e (keV); and (f) auxiliary heating power P (MW). The external power is nearly constant during this time, so confinement changes can be primarily attributed to the self-consistent evolution of profiles and turbulence. As shown, n_e rises rapidly, whereas W_{MHD} and H_{98} decrease concurrently. All diagnostics are provided at millisecond resolution. The red and black lines mark the representative times t_1 and t_2 used for subsequent spectral analyses.

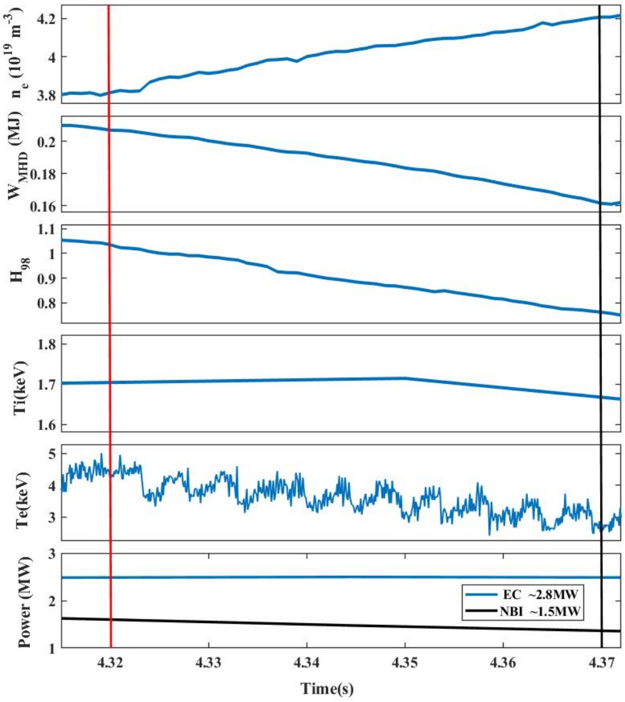

FIG. 1. Key time window of discharge #138384 (t = 0-5 s) with analysis points at 4.32 s and 4.37 s. External heating: four EC beams (total 2.8 MW) and one NBI-2R beam (1.5 MW).

Profiles at 4.32 s and 4.37 s are compared as representatives (Fig. 2a–d); the blue band marks the radial measurement region of the $\mathrm{CO_2}$-CTS system. Between the two times, n_e increases by $\sim 10.4\%$, the core T_e decreases by $\sim 30.6\%$, and T_i remains essentially unchanged, so T_e/T_i decreases markedly. Consistent with Fig. 1b–c, W_{MHD} and H_{98} both decline. This coherent evolution indicates that, under a density ramp, the overall confinement weakens and continues to deteriorate. To identify changes in turbulence drives, local gradients must be examined in detail.

As shown in Fig. 2e–h, the density and temperature gradients show differentiation around $\rho \approx 0.5$. The density gradient ∇n_e decreases, the scale length $L_{n_e} = n_e/|\nabla n_e|$ increases, and the normalised density gradient R/L_{n_e} falls from 4.11 to 3.02, indicating density profile flattening. Meanwhile, the electron-temperature gradient ∇T_e strengthens, with R/L_{T_e} rising from 6.78 to 8.90, steepening the local T_e profile. Consequently, $\eta_e \equiv L_{n_e}/L_{T_e}$ increases from 1.71 to 2.87, implying a higher relative weight of T_e-gradient drive over density-gradient drive. The combination of decreasing R/L_{n_e} and increasing R/L_{T_e} tends to weaken low-k TEM drives while strengthening high-k TEM drives. To test this correspondence, we next present the same region, broadband wavenumber spectral evidence.

Fig. 3 presents the time–frequency spectra and intensity evolution from the poloidal correlation reflectometer (PCR) and $\mathrm{CO_2}$-CTS systems. And the two channels of $\mathrm{CO_2}$-CTS cover the low-$k_\theta\rho_s$ and high-$k_\theta\rho_s$ bands,

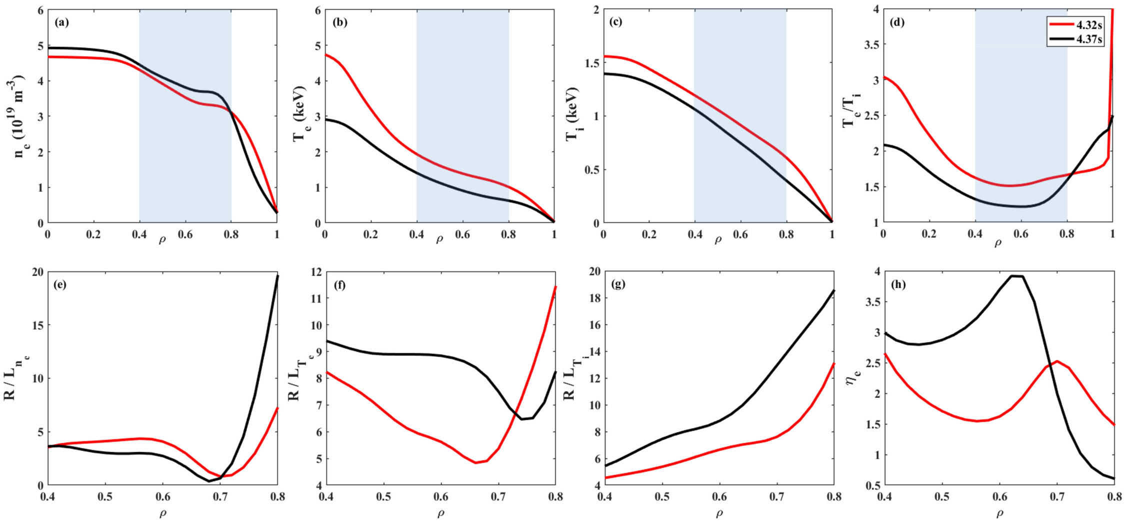

FIG. 2. Radial profiles at t = 4.32 s and t = 4.37 s: (a-d) n_e, T_e, T_i, T_e/Ti. And (e) density gradient (R/L_{n_e}), (f) electron temperature gradient (R/L_{T_e}), (g) ion temperature gradient (R/L_{T_i}) and (h) η_e profiles in discharge #138384.

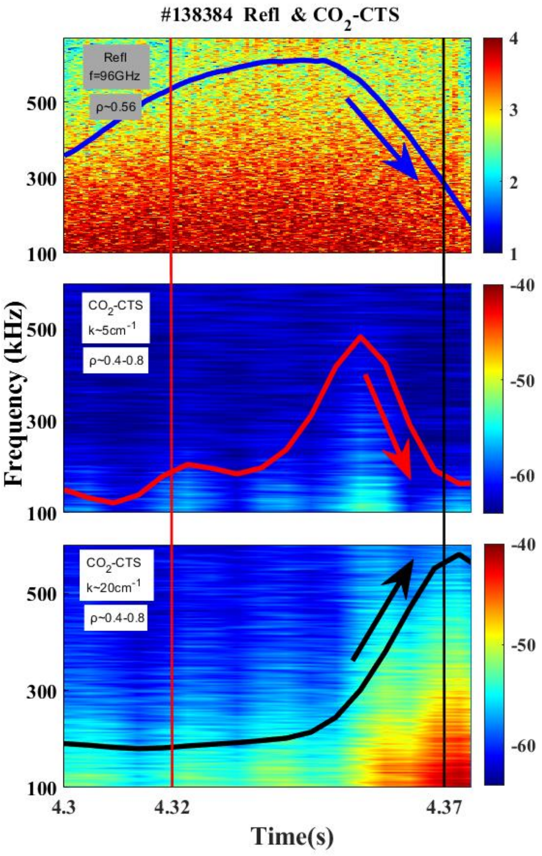

FIG. 3. Spectrograms from reflectometer and CO_2-CTS diagnostics and high-frequency band (HFB) turbulence intensity evolution.

respectively. From 4.32 s, the low-k turbulence strengthens first while the high-k turbulence lags; by 4.37 s, the low-k recedes, whereas the high-k continues to rise. The turbulence amplitude figures show that at 4.32 s, the low-k intensity (red) increases while the high-k (black) is nearly unchanged; by 4.37 s, the trend reverses. The results of PCR agree well with the CO$_2$-CTS low-k channel. The minor differences can be attributed to the fact that the k-ranges of the two diagnoses are different from each other and also vary in the radial regions. PCR accesses a smaller k ($\sim$ 0.5–1) and samples a region closer to the edge. These observations directly evidence differential evolution of multiscale turbulence within the same region: ion-scale (low-k) turbulence weakens, whereas electron-scale (high-k) turbulence strengthens; the timing is synchronous with the gradient evolution in Fig. 2.

Based on the results of the above experiment: in $T_e/T_i \sim 1$–2, R/L_{n_e} decreases, R/L_{T_e} increases, and η_e rises. Correspondingly, turbulence diagnostics observe a weakening of low-k turbulence and a strengthening of high-k turbulence. These findings provide direct evidence for an experimental picture in which TEM evolves differentially in $T_e/T_i \sim 1$–2 and shifts in tendency toward high-k electron-scale activity. The next section combines TGLF linear spectra with ONETWO inversions to identify the dominant modes and transport channels and to assess their mutual consistency.

4. SIMULATION VERIFICATION

Linear TGLF at $\rho = 0.5$ reveals a clear shift in the dominant wavenumber intervals (Fig. 4a). The trapped gyro–Landau fluid (TGLF) model enables rapid evaluation of drift-wave linear instabilities (ITG/TEM/ETG) and has been validated on multiple devices, including DIII-D and EAST. As shown in Fig. 4a, at $\rho = 0.5$, the TGLF calculations the $(\gamma/k\rho)$–$k\rho$ spectra for two times, $t_1 = 4.32$ s and $t_2 = 4.37$ s, with $k_y \approx k_\theta$ at the midplane. The shaded bands in Fig. 4a mark the two CO$_2$-CTS observation channels in the gradient region ($\rho \approx 0.4$–0.8): $k \approx 5\ \mathrm{cm}^{-1}$ ($k_\theta\rho_s \approx 0.6$–$1.0$) and $k \approx 20\ \mathrm{cm}^{-1}$ ($k_\theta\rho_s \approx 2.4$–$3.9$). Results show that at t_1 the low-k range $0.2 < k_y\rho_s < 2$ dominates the instability growth rate but is strongly reduced at t_2; conversely, the high-k range $k_y\rho_s > 1$ changes from suppressed to dominant. After normalization by $\gamma/k\rho$, the trend of decreasing low-k contribution and increasing high-k contribution remains clear and is consistent with the experimental evolution in Section 3.

For turbulence mode identification, we further use the particle flux response decomposed by $k_y\rho_s$ as the criterion (Fig. 4b). Based on linear-branch characteristics, low-$k_y\rho_s$ instability generally maps to a generalized ∇n_e-TEM, whereas the high-$k_y\rho_s$ electron-mode branch requires particle flux to distinguish ∇T_e-TEM and ETG. Comparing $\Gamma_e(k_y\rho_s)$ at t_1 and t_2, we find a clear increase in $|\Gamma_e|$ across the high-$k_y\rho_s$ range. Given that ETG typically contributes nearly zero particle flux in the quasilinear framework, whereas TEM often drives a significant and parameter-sensitive Γ_e, the enhanced high-k Γ_e is more consistent with ∇T_e-TEM than with ETG. Meanwhile, as low-k TEM weakens, the low-k Γ_e decreases markedly. Because the decrease amplitude exceeds the increase, the net effect of the particle channels after integration is reduced (with $\Gamma_e > 0$ defined as outward). Therefore, we infer that the weakening of low-k instability is primarily associated with a decline of ∇n_e-TEM, whereas the strengthening of high-k instability is mainly associated with a rise of ∇T_e-TEM. This yields a picture of "low-k TEM $\downarrow$ and high-k TEM $\uparrow$" turbulence evolution.

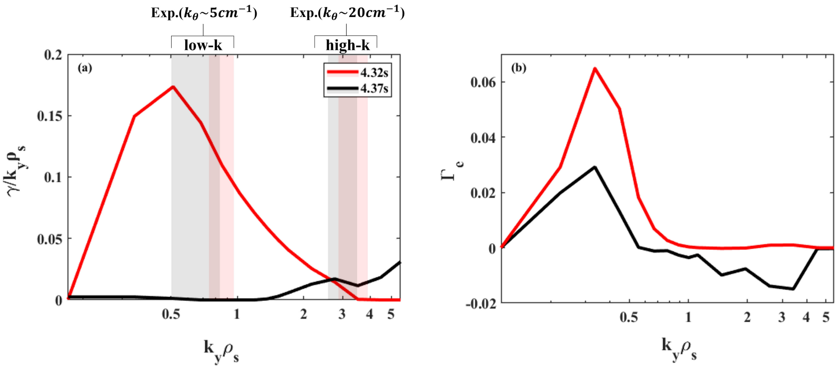

FIG. 4. The $k\rho$ spectra of (a) linear growth rates and (b) particle flux.

To assess the impact on transport channels, we utilize ONETWO inversions to obtain flux variations in a specific region (which is similar to the measurement area of PCR and CO$_2$-CTS) (Fig. 5). At $\rho = 0.5$, as low-k TEM weakens, the ion heat flux Q_i declines; as high-k TEM strengthens, the electron heat flux Q_e increases. For the particle channel, the amplitude of Γ_e decreases overall, indicating the net electron transport induced by turbulence is weakened during this time, that is, the low-k TEM is reduced. The combination $Q_e \uparrow$, $Q_i \downarrow$, and $|\Gamma_e| \downarrow$ is consistent with Section 3, where $R/L_{T_e} \uparrow$, $R/L_{n_e} \downarrow$, and $T_e/T_i \downarrow$: high-k TEM drive strengthens while low-k TEM drive weakens, manifesting as different responses in heat and particle transport.

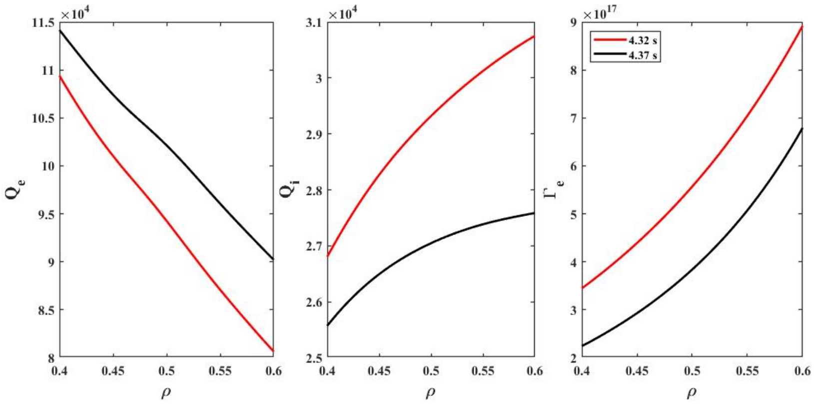

FIG. 5. Effective diffusion coefficient D_{eff} calculated by ONETWO code.

To distinguish the transport responses of different TEM, we analyze a quasilinear decomposition of fluxes by $k_y\rho_s$ using TGLF (Fig. 6). Fig. 6a compares the electron heat flux $Q_e(k_y\rho_s)$ at the two times: changes are small at low $k_y\rho_s$, whereas Q_e rises markedly at high $k_y\rho_s$, consistent with the strengthening of high-k TEM in Fig. 4a. Fig. 6b compares the electron particle flux $\Gamma_e(k_y\rho_s)$: $|\Gamma_e|$ decreases significantly at low $k_y\rho_s$, consistent with suppression of low-k TEM in Fig. 4a; only a slight increase appears at high $k_y\rho_s$. The radially integrated magnitude of Γ_e decreases overall, as shown by the ONETWO results in Fig. 5. This indicates that low-k TEM impacts the particle channel more strongly than high-k TEM, whereas high-k TEM more strongly affects the electron-heat channel. Accordingly, we infer that high-k TEM primarily drives stronger electron heat transport, whereas low-k TEM primarily drives stronger outward particle transport.

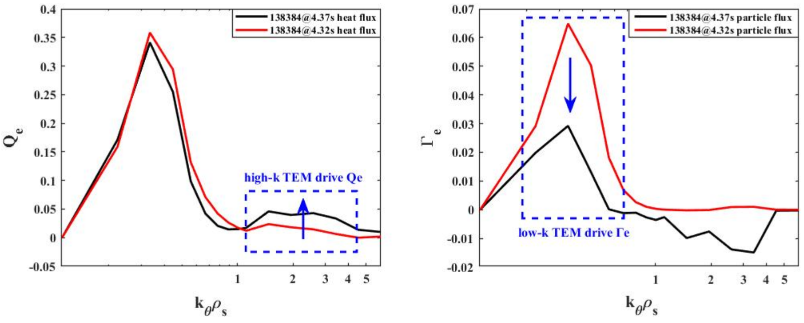

FIG. 6. High-k TEM more strongly affects the electron heat transport, and low-k TEM impacts the particle transport more strongly.

To remain descriptive rather than causal, we summarise empirical correspondences among gradients, turbulence, and transport fluxes: weakening of low-k TEM accompanies decreases in R/L_{n_e} and T_e/T_i, and is associated with the suppression of outward particle transport; strengthening of high-k TEM accompanies increases in R/L_{T_e} and η_e, and is associated with enhanced electron heat transport.To remain descriptive rather than causal, we summarise empirical correspondences among gradients, turbulence, and transport fluxes: weakening of low-k TEM accompanies decreases in R/L_{n_e} and T_e/T_i, and is associated with the suppression of outward particle transport; strengthening of high-k TEM accompanies increases in R/L_{T_e} and η_e, and is associated with enhanced electron

heat transport.

5. CONCLUSION

We directly characterise the differential evolution of TEM turbulence with $T_e/T_i \sim 1$–2 in the same region, and its dependence on profile gradients. Profiles of basic parameters show $R/L_{n_e} \downarrow$, $R/L_{T_e} \uparrow$, $T_e/T_i \downarrow$, and $\eta_e \uparrow$. Using PCR and CO$_2$-CTS systems, we achieved simultaneous observations on EAST within $\rho \approx 0.4$–0.8, covering $k_\theta \rho_s \approx 0.5$–$5$. As the line-averaged density increases, low-k turbulence weakens, whereas high-k turbulence strengthens. Simulations show that, at $\rho = 0.5$, TGLF analyzes the result of the dominant instability from low-k TEM to high-k TEM; ONETWO indicates the concurrent pattern $Q_i \downarrow$, $Q_e \uparrow$, and $|\Gamma_e| \downarrow$ in the gradient region. The three evidence lines (profiles–turbulence–transport fluxes) are self-consistent in timing, scale coverage, and spatial window, supporting that low-k TEM is more sensitive to outward particle transport, whereas high-k TEM is more sensitive to electron heat transport.

Accordingly, we propose operational insights and trade-offs for profile control: reducing R/L_{n_e} correlates with weaker low-k TEM and a marked suppression of outward particle transport; increasing R/L_{T_e} correlates with stronger high-k TEM and higher electron heat flux. Experimentally, gradient profiles can be changed by adjusting ECRH power and deposition or by optimising fueling and pumping. Combining turbulence diagnostics covering $k_\theta \rho_s \approx 0.5$–$5$ with rapid TGLF+ONETWO assessments enables the monitoring and verification of the "profiles–turbulence–transport fluxes" chain. These strategies oriented by correlation require the operational schemes to be calibrated to device constraints and diagnostic capability.

In summary, for EAST discharge #138384, we assembled a consistent evidence chain—"gradient and broad wavenumber turbulence changes $\rightarrow$ co-evolution of transport fluxes"—revealing a possibility of TEM transition from low k to high k at $T_e/T_i \sim 1$–2. And verified the consistency of experimental results, linear-stability analysis, and transport inversions. To this end, future work will pursue systematic scans of key parameters (including R/L_{n_e}, R/L_{T_e}, T_e/T_i) and effective collisionality to develop TEM classification and control windows, thereby informing active profile control for burning plasmas in CFETR and ITER.

ACKNOWLEDGEMENTS

The heading of the acknowledgements section is Times New Roman 10 point bold capitals, centred. The acknowledgements section is an optional section and can be used to list funding bodies and other sponsors of the research, and to mention people who supported the research but whose contribution was not of a type to merit authorship of the paper.

REFERENCES

[1] ANGIONI, C., Plasma Phys. Control. Fusion **51** 124017 (2009).

[2] ANGIONI, C., Phys. Plasmas **10** 3225 (2003).

[3] ARNICHAND, H., Plasma Phys. Control. Fusion **58** 014037 (2016).

[4] ARNICHAND, H., Nucl. Fusion **55** 093021 (2015).

[5] ARNICHAND, H., Nucl. Fusion **54** 123017 (2014).

[6] BAI, L., Chin. Phys. Lett. **12** 743 (1995).

[7] BANERJEE, D., Nucl. Fusion **57** 076005 (2017).

[8] BAVER, D. A., Phys. Plasmas **9** 3318 (2002).

[9] BELLI, E. A., Plasma Phys. Control. Fusion **65** 024001 (2023).

[10] BELLI, E. A., Plasma Phys. Control. Fusion (2024).

[11] BERNARDO, J., Plasma Phys. Control. Fusion **57** 035002 (2015).

[12] BOURDELLE, C., Nucl. Fusion **54** 022001 (2014).

[13] CASATI, A., Phys. Plasmas **15** 042310 (2008).

[14] CHAPMAN-OPLOPOIOU, B., Nucl. Fusion **62** 086028 (2022).

[15] CHEN, F., Plasma Sci. Technol. **25** 085102 (2023).

[16] CHEN, H., Phys. Rev. Lett. **128** 025003 (2022).

[17] CHEN, J., Nucl. Fusion **64** 086054 (2024).

[18] CHEN, L., Phys. Rev. Lett. **92** 075004 (2004).

[19] CHEN, Y., Plasma Phys. Control. Fusion **56** 105006 (2014).

[20] CITRIN, J., Plasma Phys. Control. Fusion **59** 064010 (2017).

[21] CITRIN, J., Nucl. Fusion **62** 086025 (2022).

[22] CONNOR, J. W., Plasma Phys. Control. Fusion **48** 885 (2006).

[23] DANNERT, T., Phys. Plasmas **12** 072309 (2005).

[24] DIMITS, A. M., Phys. Plasmas **7** 969 (2000).

[25] DRAKE, J. F., Phys. Rev. Lett. **44** 994 (1980).

[26] ERNST, D. R., Phys. Plasmas **11** 2637 (2004).

[27] ERNST, D. R., Phys. Plasmas **23** 056112 (2016).

[28] ERNST, D. R., Phys. Plasmas **16** 055906 (2009).

[29] FROULA, D., Phys. Rev. Lett. **98** 135001 (2007).

[30] GALANTE, M. E., Nucl. Fusion **55** 123016 (2015).

[31] GARBET, X., Phys. Rev. Lett. **91** 035001 (2003).

[32] GAUR, R., J. Plasma Phys. **89** 905890112 (2023).

[33] GENG, J. S., Sci. Rep. **15** 7738 (2025).

[34] GORLER, T., Phys. Rev. Lett. **100** 185002 (2008).

[35] GORLER, T., J. Comput. Phys. **230** 7053 (2011).

[36] HAHM, T. S., Rev. Mod. Plasma Phys. **8** 30 (2024).

[37] HAN, H., Nature **609** 269 (2022).

[38] HATCH, D. R., Nucl. Fusion **64** 066007 (2024).

[39] HE, Y. F., Nucl. Fusion **64** 076064 (2024).

[40] HORTON, W., Rev. Mod. Phys. **71** 735 (1999).

[41] HOSOGANE, N., Nucl. Fusion **28** 1781 (1988).

[42] HOWARD, N. T., Phys. Plasmas **23** 056109 (2016).

[43] HU, Y. C., Plasma Phys. Control. Fusion **65** 055023 (2023).